Heat transfer investigation near the onset of nucleate boiling on a single artificial nucleate site: Influence of the wall orientation

Himanshi Kharkwal^{1,2}, Mohammed Zamoum³, Magali Barthès¹, François Lanzetta², Hervé Combeau⁴ and Lounès Tadrist⁵

- ¹ Université Marie et Louis Pasteur, CNRS, institut FEMTO-ST, F-25000 Besançon, France
- ²Université Marie et Louis Pasteur, CNRS, institut FEMTO-ST, F-90000 Belfort, France
- ³ Université M'hamed Bougara, Laboratoire LGPH, Boumerdes, Algeria
- ⁴ Université de Lorraine, CNRS, Institut Jean Lamour, Nancy Cedex, France
- ⁵Université d'Aix-Marseille, CNRS, IUSTI, Marseille, France

Corresponding author: himanshi.kharkwal@univ-fcomte.fr

Abstract

Studying the transition from natural convection to nucleate boiling is crucial for both the efficiency and safety of thermal systems. Present study aims to investigate the heat transfer characteristics at the transition of the natural convection and the nucleate boiling regimes. An experimental setup has been designed and implemented to perform experiments with FC72 on flat heating wall that can be inclined from 0° to 180° . This was possible thanks to the development of a boiling meter mounted on a pivoting axis. This work provides new insights into local wall heat transfer behavior and nucleation dynamics under varying gravitational configurations, contributing novel data on single-site boiling physics. Intermittent behavior with typical heat transfer cycles is evidenced. Two criteria are found to control this intermittency; the wall temperature threshold for bubble nucleation and the heat flux threshold needed to sustain bubble emission. A single nucleation site leads to a variation in the transfer coefficient. Changing inclination from 0° to 180° increases the heat transfer coefficient in the bubble emission regime from 263 to $489 \ W/m^{2\circ}C$ but decreases it in natural convection from 240 to $176 \ W/m^{2\circ}C$.

Keywords: Pool boiling, natural convection, transition regime, heat transfer coefficient, single nucleation site, surface inclination

Nomenclature

Symbols

Т

h Heat transfer coefficient $(W/m^2 \circ C)$ P Pressure (bar)P_c Critical power (W)q Heat flux (W/m^2)

Temperature (${}^{\circ}C$)

 ΔT Wall superheat (°*C*)

t time (s)

 T_L Liquid temperature

 T_{sat} Saturation temperature (°C)

 T_W Surface temperature (°C)

 θ Surface inclination (°)

 τ_{BER} Characteristic time for bubble emission regime (s)

 τ_{LNC} Characteristic time for liquid natural convection (s)

 $au_{trBER-LNC}$ Transition time from bubble emission regime to liquid natural convection regime

(s)

 $au_{trLNC-BER}$ Transition time from liquid natural convection regime to bubble emission regime

(s)

Abbreviations

BER Bubble emission regime

LNC Liquid natural convection

ONB Onset of nucleate boiling

1. Introduction

The ongoing trend of electronic device miniaturization has significantly increased the need for advanced thermal management solutions. Among various passive heat transfer enhancement techniques, nucleate boiling has gained considerable attention due to its high heat transfer efficiency [1]. This efficiency is primarily attributed to the formation of vapor bubbles within microcavities or on roughened heating surfaces, which actively disrupt the thermal boundary layer and enhance heat removal. Due to its broad applicability and potential for energy optimization, boiling has been the subject of intensive research for several decades. A major objective of these studies is to identify and optimize key parameters that lead to enhanced heat transfer performance [2-4]. Research efforts span several domains, including surface modification, where changes to surface roughness [5], patterning [6], coatings [7], or the integration of micro and nanostructures are used to promote bubble nucleation and detachment [8]. Another important area involves fluid property enhancement, such as the use of nanofluids, additives, or phase-change materials to improve thermal conductivity and boiling characteristics [9,10]. Additionally, system-level and geometric optimization- particularly in the design of flow channels, orientation, and confinement structures- plays a crucial role in maximizing boiling heat transfer efficiency under various operational conditions [11,12].

Although extensive research has been conducted to optimize boiling heat transfer, the presence of multiple interacting bubbles introduces significant complexity, making it challenging to fully understand the underlying mechanisms. The dynamic interactions between bubbles, surface conditions, and fluid properties create a highly transient and non-linear environment [13]. To address this, different studies are conducted on single-bubble investigations, which offer a more controlled framework for isolating and analyzing fundamental processes at the microscale level. For instance, Di Marco et al. [14] experimentally measured the rising velocity of bubble after detachment, showing gaps in the available models, and Vasquez et al. [15] compared three measurement techniques for the determination of the bubble size at detachment. Moghaddam and Kiger [16] have studied the dynamics of heat transfer during nucleation process of saturated FC-72 liquid. They determined the time period of activation, area of influence, and magnitude of three different mechanisms of heat transfer at the nucleation site. These mechanisms included microlayer evaporation that occurred during the rapid expansion of bubbles, transient conduction resulting from the rewetting of the surface as bubbles departed, and micro convection taking place in the area surrounding the bubblesurface contact region. Li et al. [17] performed pool boiling tests with binary mixtures: their findings suggest that, in comparison with pure fluids, bubble growth in binary mixtures starts off more slowly but accelerates more rapidly over time. Effect of pressure on nucleate pool boiling was studied by Kumar et al. [18]. The experiments were conducted on a single nucleation site created on a copper substrate, further testing water at three pressure conditions. The results show that the decreasing pressure alters the forces acting on a bubble, leading to the creation of larger bubbles, which was previously observed in the studies of Stralen et al. [19] and Kim et al. [20]. Furthermore, numerous experimental and numerical studies have been devoted to understanding the thermal and hydrodynamic interactions during single-bubble boiling events. Early investigations by Rogers and Mesler [21] and Hendricks and Sharp [22] highlighted that surface temperature declines during bubble growth and recovers upon detachment, attributing heat transfer primarily to evaporation from thin liquid films, rather than micro convection or bulk liquid quenching. Subsequent studies refined this understanding by linking local temperature changes to specific bubble dynamics. Tsai and Lin [23] demonstrated that bubble nucleation and surface cooling on micro-resistors are highly dependent on input current levels, as no nucleation was observed at low levels, while intermediate currents led to delayed single-bubble nucleation accompanied by a temperature drop. After bubble formation, the resistor temperature gradually increased and stabilized. Demiray and Kim [24] further emphasized the role of microlayer evaporation in enhancing heat flux during growth. They observed that during the nucleation and growth stages of a bubble, heat flux increases. They attribute this rise to the evaporation of the thermal microlayer between the bubble and the heated surface. As the bubble reaches its maximum diameter and begins to detach from the wall, a decline in heat flux is noted. This reduction is linked to wall overheating caused by the continued evaporation of the microlayer. On the contrary, Myers et al. [25] and Golobic et al. [26] identified transient conduction and surface rewetting as critical contributors to peak heat transfer at bubble departure. Myers et al. [25] used several platinum micro-resistors to study heat transfer under constant heat transfer conditions. They showed that the wall temperature reached its maximum as the dry spot under the bubble also reached its maximum. Then the temperature dropped abruptly since the rewetting of the surface led to an increase in heat flux, which peaked again when the bubble departed. They identified transient conduction during the departure of the bubble as the main factor contributing to heat transfer. Golobic et al. [26] experimentally determined the transient wall temperature distributions close to the growing vapor bubbles. They observed that under conditions of constant imposed heat flux, the wall temperature decreases as the bubble expands. They conclude that the growing bubble extracts heat from the wall during its development. Quantitative insights were added by Yabuki and Nakabeppu [27] and Jung and Kim [28], who measured microlayer evaporation's contribution to be 17–50%, with the remainder attributed to heat transfer through the surrounding superheated liquid. These findings were confirmed by numerical studies. Li et al. [29] demonstrated sharp temperature drops near the contact line via multi-cycle simulations, while Li et al. [30] validated numerical models against experimental data, confirming that microlayer evaporation can dominate bubble growth, especially at moderate wall superheats. In the study of Cao et al. [31] the results show that vapor inside the bubble is superheated, wall superheat accelerates bubble departure and enlarges its diameter, and spatially averaged heat flux peaks at bubble departure before gradually declining.

Based on the above studies, even in the case of single bubble growth, the underlying mechanisms remain under investigation, with no definitive conclusions yet established. This is largely due to the limited understanding of the wall-level phenomena and the scarcity of literature focused on single-site bubble behavior. Most of the work on single-site boiling has focused on bubble dynamics. It is difficult to distinguish from these works the dominant phenomena in bubble growth. For example, according to some authors, evaporation of the micro-layer of liquid under the bubble is the main cause of heat transfer into the liquid film [24,30] while for others, evaporation is mainly induced at the contact line [32]. In these studies of steam bubble growth, the characteristic time involved is that of bubble formation. Boiling involves phenomena with several characteristic times. In addition to the bubble's lifetime from nucleation to detachment, the characteristic times of the heating wall and of the surrounding liquid needs to be considered. Given the phenomena involved, these characteristic times differ significantly from those of bubble dynamics.

Over the past few years, we have been studying boiling by taking into account all the characteristic timescales associated with the boiling phenomenon. Experimental studies by Zamoum et al. [33], Tadrist et al. [34] and Kharkwal et al. [35] provide valuable insights into pool boiling heat transfer mechanisms, with a focus on the effects of wall orientation and nucleation site characteristics. Using Fluorinert FC72 as the working fluid, each study employed a specially designed boiling meter capable of measuring local heat flux and wall temperature under controlled conditions. Zamoum et al. [33] reported first experiments for single and multiple nucleation sites. They demonstrated that single nucleation site studies allowed detailed visualization and quantification of individual bubble growth and departure cycles. For multiple nucleation sites, it was shown that the experimental setup was able to produce data on the heat transfer characteristics thanks to the boiling meter. It has been also possible to determine the onset of nucleate boiling (ONB) as a function of the wall orientation. Tadrist et al. [34] investigated heat transfer characteristic curves for natural multiple bubble at different wall inclination. When increasing imposed heat flux, they characterized the onset of nucleate boiling (ONB) and for decreasing imposed heat flux they determined the onset of natural convection (ONC) as functions of wall orientation. Their findings revealed that both ONB and ONC superheats decrease with increasing inclination, and that heat transfer behavior varies depending on the imposed heat flux. Kharkwal et al. [35] focused on boiling on single artificial nucleation site. They demonstrated that alternating activation and deactivation cycles are present across all tested surface inclinations (0°-180°). Notably, they observed that the nucleation site becomes more active when reaching 180° inclination angle. For this inclination, the nucleation site remains almost continuously active but exhibits highly unstable emission behavior. Across these three studies, the boiling meter proved essential for capturing transient thermal behaviors and offered a more nuanced understanding of boiling phenomena beyond classical steady-state models.

In the present study, we focus on the onset of nucleate boiling (ONB) at a single nucleation site, a novel approach compared to previous works. Our emphasis lies in examining the thermal behavior of the wall during bubble activity and, more importantly, in understanding the transition from natural convection to the nucleate boiling regime. By analyzing heat flux and wall temperature variations during this transition, we provide new insights into the mechanisms governing ONB at both the local and global scales. To achieve these objectives, we focus our investigation on analyzing the influence of wall orientation on the dynamics of boiling and the associated heat transfer on a single artificial nucleation site for four inclination angles (180°, 179°, 90° and 0°) of the wall. The natural convection regime varies from a thermal plume regime for the 0° orientation to a convection cell regime whose intensity decreases sharply with increasing wall inclination. Similarly, bubble dynamics vary with wall orientation. Bubble diameter, growth and detachment frequency are highly dependent on wall orientation. The forces acting on a bubble and the interaction with the wall vary significantly for these four typical orientations.

The paper is organized in three following sections. In the second section, the experimental setup, the material and the methods are presented. The third section details the results, through both heat flux and wall temperature measurements. In this section heat transfer analysis is also carried out using an analytical model to analyze the intermittent thermal behavior induced by the activation and deactivation of the artificial nucleation site. The heat transfer coefficient is deduced from the experimental results. The last section is dedicated to the conclusion where the main findings are summarized and prospects for this work are given.

2. Experimental setup

The experimental setup (Figures 1(a) and 1(b)) allows to perform pool boiling experiments on a smooth surface, with fixed thermal conditions. Details on the experimental setup and protocol are given in sections 2.1 and 2.2, respectively.

2.1. Test cell and its instrumentation

The test cell constitutes a cubic enclosure of 100 mm side. The structure of the cell is in Teflon with faces in plexiglass. The wall thickness is 10 mm. Teflon and plexiglass are weak heat conductor, thus, the thermal losses are minimized. Furthermore, being transparent, plexiglass also allows to visualize the dynamics of the boiling. This cell is conceived to be tight in the range of absolute pressures going from 0.1 bar to 2 bar. The experiments are carried out at saturation conditions, thus the two phases (liquid in the bottom of the cell, vapor on the top) are present. To control and maintain the liquid at desired saturation temperature during the experiment, the cell is equipped with a heating cartridge and with a cooling coil in which a fluid circulates.

To create the boiling surface and measure the thermal parameters (heat flux and surface temperature), a boiling meter was implemented. Its fabrication and calibration are detailed in [33,34]. The specifications are shown in Figure 1(c). Let's briefly review the various components. A 30 μ m thick heating resistor is placed in the center of the boiling meter. Two 2

mm thick copper pellets are placed on either side of the heating resistor. Two $400\,\mu m$ thick heat flux meters are then placed on top of these copper pellets. Each component is joined to the next by an adhesive layer approximately $50\,\mu m$ thick. The lower face of the boiling meter is insulated with a 1 mm thick rubber pad. On the upper face of the boiling meter is the boiling surface. On the side of the boiling meter is a $400\,\mu m$ thick heat flux meter and a 5mm thick resin pad for thermal insulation.

More specifically, the heat fluxes are measured by two circular Captec heat flux sensors [36], with diameter 20 mm, and having a sensitivity of $2.82 \pm 0.2 \,\mu V/W/m^2$. The heat flux sensors used are a tangential thermal gradient one [37]. They are made up of planar thermopile distributed over its entire surface. The heat flux measurement therefore corresponds to the heat flux crossing through the entire wall surface. To create a single nucleation site at the center of the boiling surface, an artificial nucleation site is created by drilling with a 200 μ m diameter drill bit to a controlled depth of 150 μ m. The resulting artificial nucleation site has an average diameter of 200 μ m and a depth of 150 μ m [33,34]. Further, for measuring the surface temperature, a T type thermocouple is placed just under the top copper layer of each heat flux sensor. This thermocouple was calibrated using a PT-100 sensor with an accuracy of ± 0.03 °C within the 0°C to 60°C temperature range. The combined type-B uncertainty in temperature measurements is 0.2 °C (see Appendix 1).

This thermocouple allows the local wall temperature measurement. Since the thermocouple is located just below the nucleation site, it detects the thermal variation at less than 100 μ m below the site. It is therefore a point detection, and sensitive to the local behavior of the fluid and the wall at the measurement point. The acquisition frequency of all the measured variables is 5 Hz. Boiling meter was used to create boiling with varying surface inclination. The surface is tilted by the rotating shaft. Tilt angles are determined to an accuracy of $\pm 0.5^{\circ}$.

In the vapor zone, a condenser allows the vapor condensation and to maintain the enclosure under the conditions of saturation. To evacuate non-condensable gases, a reflux condenser has been installed on the top face of the enclosure. The core pipe connected to the enclosure at an extremity is occupied by the vapor and non-condensable gases coming from dissolved gas in the liquid phase. The opposite extremity is connected to the atmosphere by a valve to eliminate the non-condensable gases. In the annular zone, the cooling liquid allows to condense only the vapor and thus to separate it from non-condensable gases.

Fluorinert FC72 (3M TM) has been chosen as test fluid to study the boiling phenomena. It is thermally and chemically stable, its boiling point is relatively low (56.6 $^{\circ}$ C at 1 bar) and its latent heat is 93096 J/kg at 25 $^{\circ}$ C [38]. A magnetic stirrer is placed at the bottom of the enclosure and allows homogenizing the temperature of the liquid when it is necessary, notably at the beginning of one experiment before activation of the boiling cell. Four calibrated thermocouples of K type placed in the enclosure allow the measurement of the fluid temperature. Pressure in the enclosure is measured by the SCX 15DN pressure sensor that has \pm 1% pressure accuracy over a wide temperature range. This sensor is calibrated and temperature compensated, to provide a stable output signal within the temperature range of 0 $^{\circ}$ C to + 85 $^{\circ}$ C. The sensors have an absolute pressure measurement range from 0.1 bar to 2 bar.

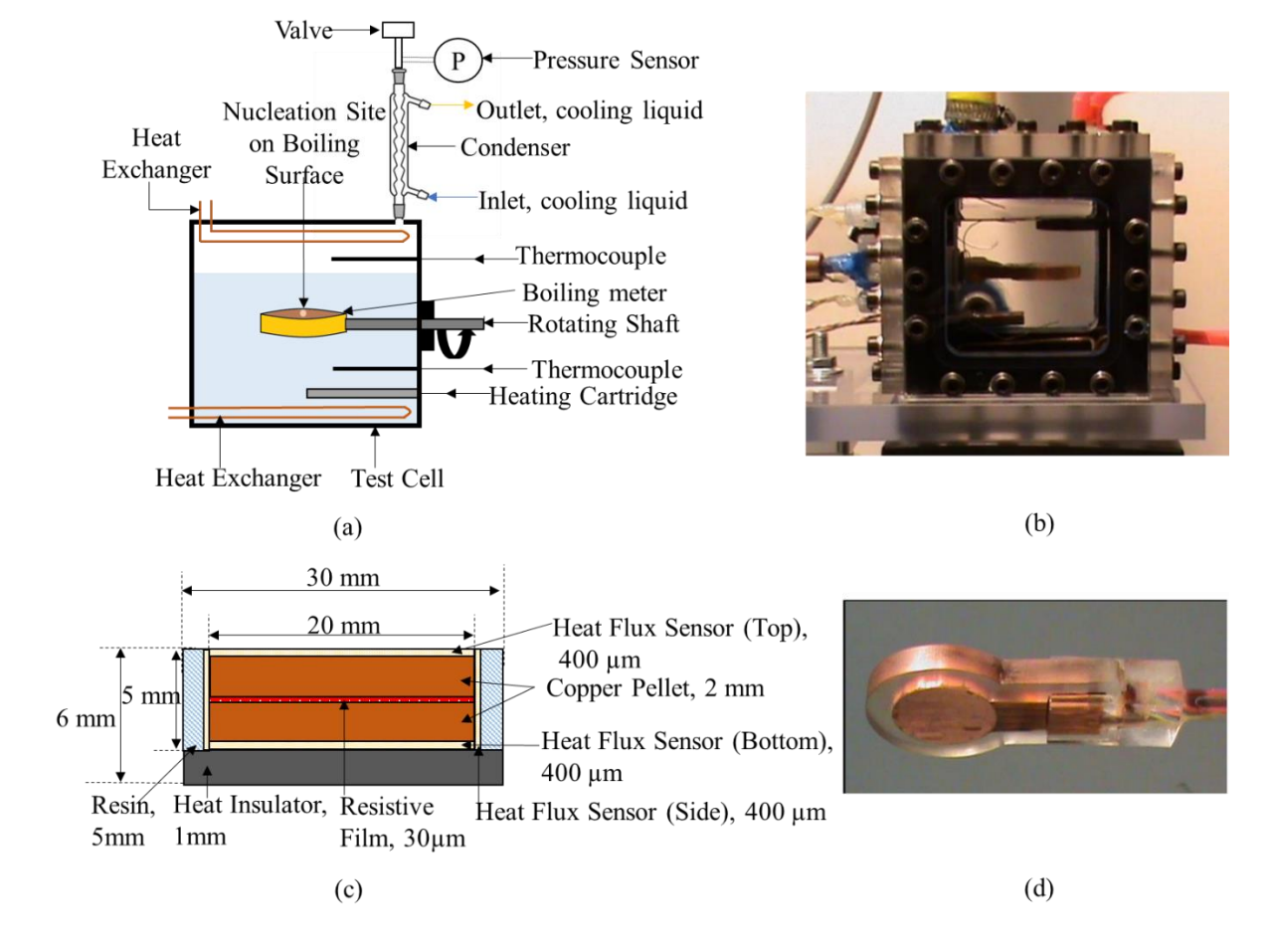


Figure 1 (a) Schematic of the experimental setup consisting of the boiling cell, boiling meter along with sensors for measuring temperature and pressure. Two heat exchangers are incorporated to regulate the temperature in both the liquid and vapor phases; (b) Photograph of the boiling chamber (c) Illustration showing the vertical section of the boiling meter, detailing its components with dimensions. The reflective section serves as the active boiling surface, while a thick Teflon piece adhered to the opposite side deactivates the symmetrical surface. The periphery of the boiling meter is encased in insulating resin to prevent boiling in that area; (d) Photograph showing side view of the boiling meter [35].

2.2. Experimental protocol

Before starting the experiment, a dedicated degassing procedure was adopted. Firstly, the cell was filled with the working fluid Fluorinert (FC72), and further the degassing was performed. The procedure consists in heating gradually the liquid by using the immersed heating cartridge while stirring the liquid by using a magnetic agitator. After a while, the temperature and the pressure increase in the cell. As soon as the liquid borders the conditions of saturation, there are formation of vapor and degassing of the liquid. The mixture of vaporair reaches the top part of the enclosure surmounted by a condenser in which circulates a cooling liquid. An important fraction of the vapor is then condensed, while the other fraction mixed with non-condensable gases is evacuated outside the enclosure through the reflux condenser by a manual opening of the valve. This operation is repeated several times until the thermodynamics conditions corresponding to the state of saturation of the pure fluid has been

reached. The heating of the enclosure by the cartridge is then stopped. The fluid cooled naturally until the desired temperature. As the enclosure is tight and that the fluid is in saturation state, then the decrease of the temperature leads to decrease the pressure.

Then, to investigate the phenomena, we first bring the fluid to the desired saturation temperature, using the cartridge heater for saturation temperatures above room temperature and the heat exchangers for temperatures below room temperature. For saturation temperatures equal to room temperature, both elements are not activated. Once the saturation temperature has been reached and is homogeneous in the liquid and vapor phases, the resistive film at the center of the boiling meter is used to progressively supply heat by the Joule effect. The thermodynamic and thermal data are recorded: wall, liquid and vapor temperatures, the heat flux crossing the surface and the pressure in the cell. Bubble dynamics are recorded by a video camera.

Once the stationary state has been reached and data recorded for a given wall inclination, a new angle is imposed. The system then transits to a new thermal state. All thermodynamic quantities are kept constant throughout the experiments (fluid temperature and pressure). All measured data are recorded and processed in a later phase. In the following section, we present the experimental results obtained for a selection of four wall orientations: 0° , 90° , 179° , 180° . 0° corresponds to a bubble created on the surface (surface facing upwards) and 180° corresponds to a bubble created below the surface. The 180° orientation is the initial orientation from which the experiment is initiated.

3. Results

This section covers the experimental results performed in the present study. Heat transfer between the heated wall and the liquid under conditions close to saturation conditions was investigated. In the first part, details on the effect of the surface orientation on thermal parameters, heat flux and wall temperature, are presented. In the second part, heat transfer curves are deduced and analyzed.

3.1 Fluid flow behavior at the wall: Activation and deactivation of a bubble nucleation

As mentioned before, the heat flux values are obtained from the heat flux sensor. They correspond to the heat flux crossing the total area of the heated surface (3.14 x 10^{-4} m²); while the temperature measurements are given by the T type thermocouple located underneath the nucleation site at approximately 100 μ m.

Once the fluid saturation conditions are obtained, the experiments start with the surface inclination of 180° . Subsequently a progressive increase in heating power was imposed. At this configuration, with a critical heating power P_c equal to 0.462 ± 0.005 W, the nucleation site becomes active. The latter remains active during all the experimental time. Figure 2 shows, the time series of the wall temperature measured with a thermocouple just under the nucleation site and the heat flux measured at the wall. Each period corresponds to one bubble: it's nucleation, growth and detachment. The behavior is cyclic, without deactivation of the nucleation site. Thanks to the video analysis, frequency of the bubble emission was determined which is 0.7 Hz. To ease the reading of the curves, error bars on Figure 2 and 3 are given only on few data points.

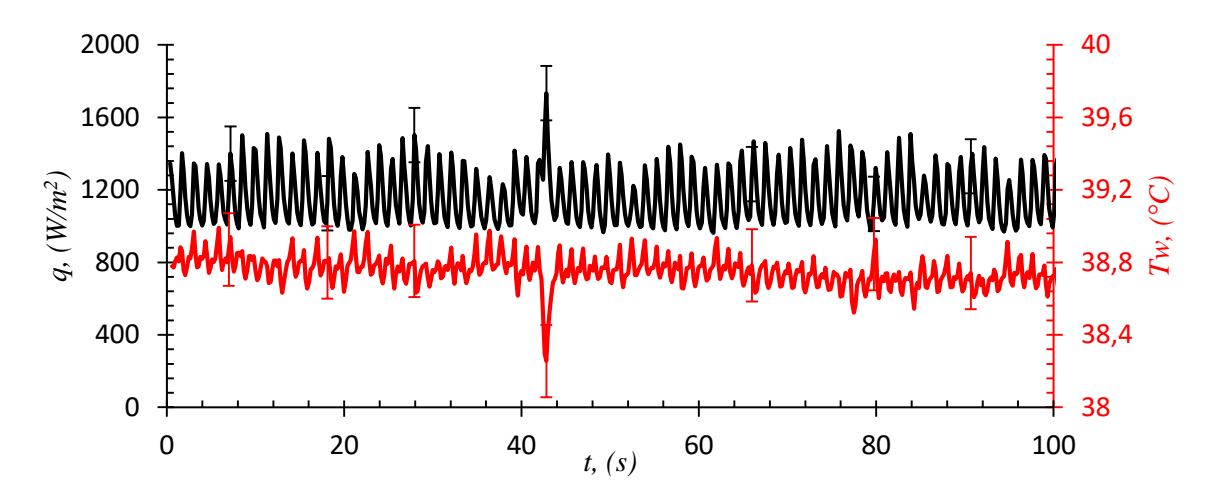


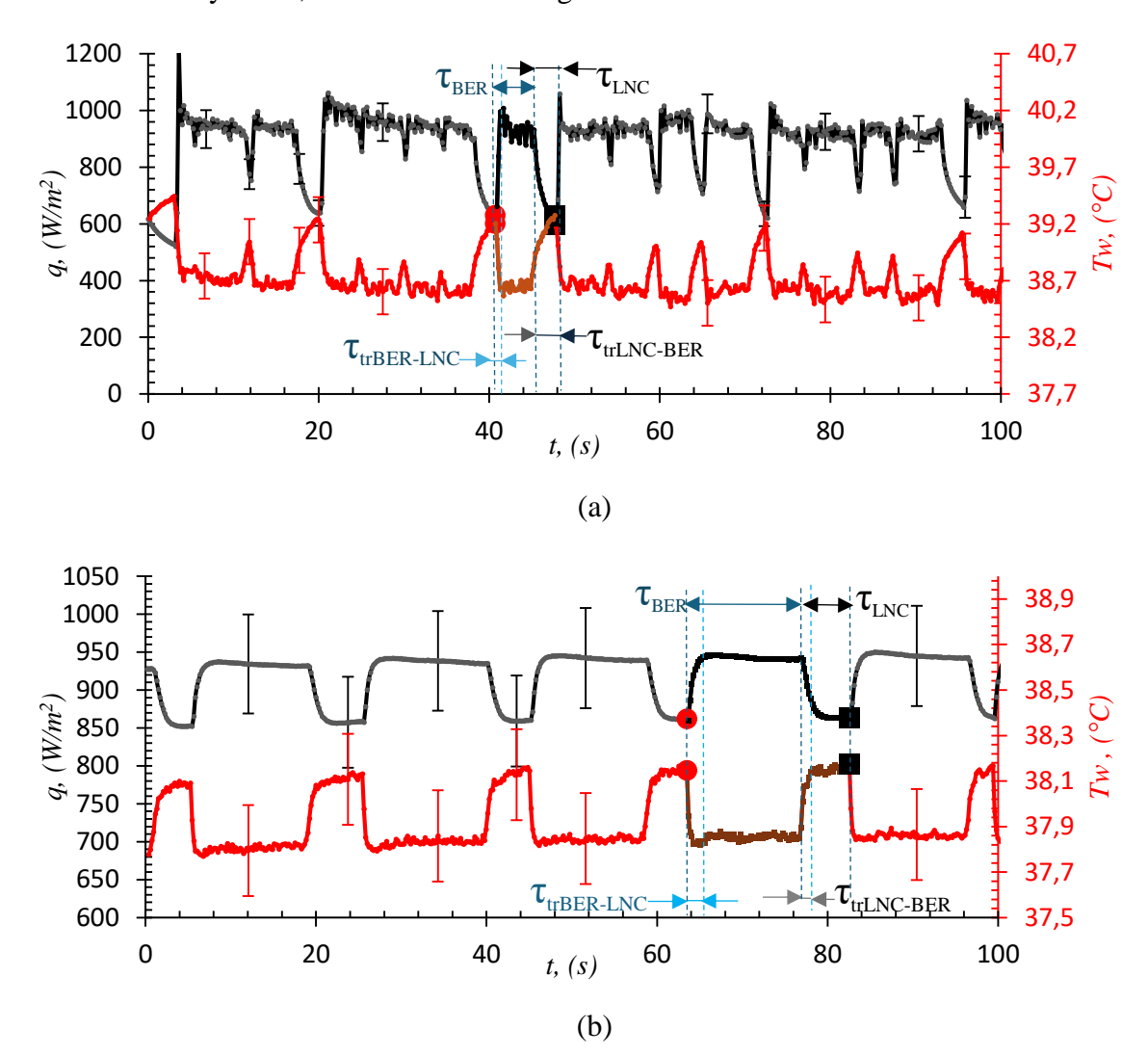
Figure 2 Variation of heat flux q (in black) and wall temperature T_w (in red) with time t for surface inclination $\theta=180^\circ$, at critical heating power $P_c=0.462\pm0.005\,W$; $P_{sat}=0.47\,\mathrm{bar}$; $T_{sat}=36.4\,^\circ\mathrm{C}$. The mean heat flux is 1200 W/m² with a fluctuation of $\pm200\,\mathrm{W/m^2}$ and mean wall temperature is $38.75\,^\circ\mathrm{C}$

Further, maintaining the imposed power of 0.462 W, the surface orientation was changed to 179°. For this orientation, we observe an intermittent behavior at the wall; which is characterized by a period where the nucleation site is active, bubble emission occurs on the artificial nucleation site, and a period where the nucleation site becomes inactive. In addition to the observation, this effect is evidenced by the heat flux and temperature at the wall. Figure 3 (a) shows the time series of the heat flux and temperature at the wall. It can be noticed that there exist two thermal behaviors: in one period of the cycle, the wall temperature is almost constant at 38.5°C, with an average heat flux density of around 960 W/m². In another phase, the temperature rises steadily until it reaches a temperature of 39.2°C. In this phase, the heat flux density decreases until it reaches a minimum value of 560 W/m². Once these temperature and flux conditions have been reached, there is an abrupt decrease in wall temperature and an increase in heat flux, returning to the conditions of the previous cycle. Observations made using video imaging show that this intermittent phenomenon is linked to continuous activation of the nucleation site during the first period, followed by an extinction period of the nucleation site during the second phase.

During the activation phase, the bubbles nucleate, grow and detach from the wall, cross the liquid and enter the vapor space at the top of the boiling cell. At this phase, small fluctuations in temperature and heat flux are observed, corresponding to successive bubble emissions. For simplicity, the regime when the nucleation site is active is referred as bubble emission regime (BER); and the second regime corresponds to an inactive nucleation site, which is referred as liquid natural convection regime (LNC). Thus, τ_{BER} corresponds to the total time in which nucleation site is active and bubble emissions are continuous, and τ_{LNC} corresponds to the time in which nucleation site is inactive and heat transfer is mainly through liquid natural convection. $\tau_{trBER-LNC}$ and $\tau_{trLNC-BER}$ are the transition times taken between changing regimes from BER to LNC and LNC to BER respectively.

Similar time series were established for wall orientations of 90° and 0°. The intermittent behavior evidenced for an inclination of 179° persists regardless of wall orientation, with different behaviors depending on the angle of inclination. For an inclination of 90° (cf. Figure 3 (b)) the bubble emission is visible during a time interval alternating with no bubble emission.

The bubbles slide along the heated wall, their size and emission time period varied strongly as a function of the boiling wall inclination. The time series of wall temperature and heat flux highlight a periodic behavior between BER and LNC with steady state for the two regimes (Figure 3 (b)). For an inclination of 0° (cf. Figure 3 (c)), upward facing wall, the bubbles nucleated in the center of the boiling meter, grew and due to the gravity action, detached from the heated wall. For this inclination, even if the nucleation site is inactive (i.e., at LNC), the wall heats the fluid and, due to the density difference, the heated fluid rises and thus causes fluid motion in the form of plumes. When the bubble nucleation events occur (BER), as the bubble size is very small, it adds a small change in the heat flux values.



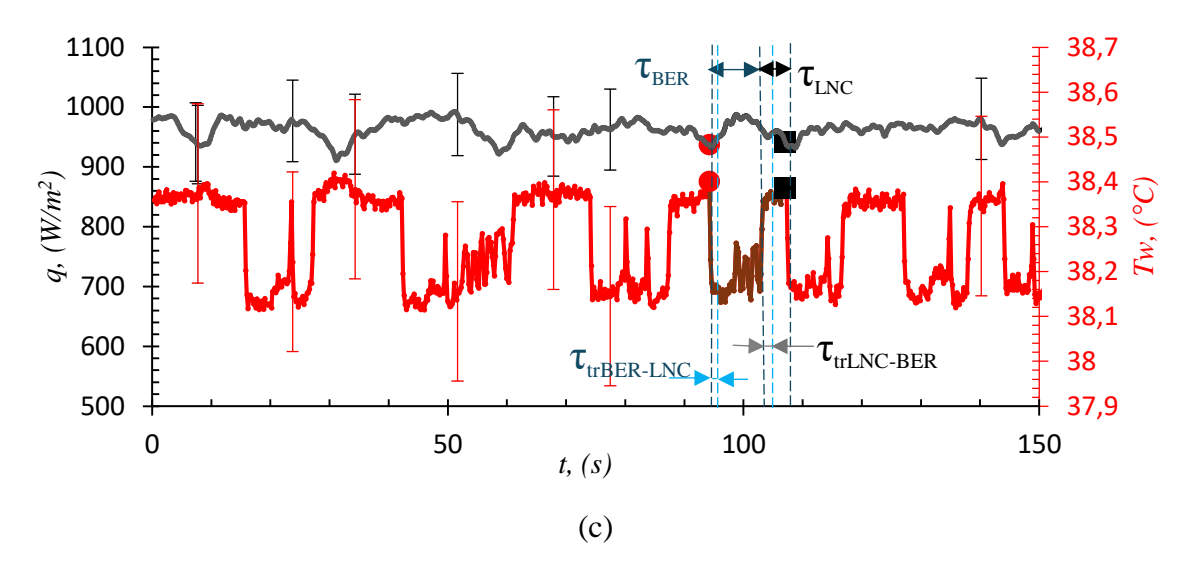


Figure 3 Heat flux and wall temperature variations at surface inclinations of (a) $\theta = 179^{\circ}$, $P_{sat} = 0.46 \ bar$, $T_{sat} = 35.7^{\circ}C$, (b) $\theta = 90^{\circ}$, $P_{sat} = 0.44 \ bar$, $T_{sat} = 34.6^{\circ}C$, and (c) $\theta = 0^{\circ}$, $P_{sat} = 0.44 \ bar$, $T_{sat} = 34.6^{\circ}C$. The plots highlight the characteristic times τ_{BER} and τ_{LNC} corresponding to BER and LNC regimes, as well as the transition times between these regimes, denoted as $\tau_{trBER-LNC}$ and $\tau_{trLNC-BER}$

It is noticed that the period of each regime differs with the inclination (Table 1). For an inclination of 179° the BER period ($\tau_{BER} = 5.2s$) is three times higher than the LNC period ($\tau_{LNC} = 1.7s$). For 0° wall inclination the BER period remains higher ($\tau_{BER} = 11.7s$) but close to the LNC ($\tau_{LNC} = 9.6s$). Furthermore, by performing the video analysis, bubble emission time (τ_b), which is the total time taken by one single bubble to nucleate-grow-depart was evaluated. The increase in bubble emission time with increasing surface inclination from 0° to 179° can be noticed in Table 1.

Table 1 Characteristic times for BER τ_{BER} and LNC regimes τ_{LNC} regimes and the transition time between the two regimes ($\tau_{trBER-LNC}$ and $\tau_{trLNC-BER}$). These two times and shown in Figures 3 (a), (b) and (c). Bubble emission time τ_b for each inclination.

θ	$ au_{BER}(s)$	$\tau_{LNC}(s)$	$ au_{trBER-LNC}(\mathbf{s})$	$\tau_{trLNC-BER}(s)$	$\tau_b(s)$
0°	11.7	9.6	0.9	0.8	0.04
90°	13.6	5.2	2.8	3.4	0.07
179°	5.2	1.7	2.5	0.5	0.3

Comparing the three surface inclinations studied, it is observed that the heat flux values at BER across all inclinations show minimal variation, ranging between q = 920 and $1020 \, W/m^2$. However, the heat flux at LNC varies significantly with surface inclination. At LNC, the lowest heat flux is observed at $\theta = 179^{\circ}$, and it increases progressively as the inclination approaches $\theta = 0^{\circ}$. Consequently, the difference in heat flux value between BER and LNC is greater at $\theta = 179^{\circ}$ and decreases as the surface inclination moves toward $\theta = 0^{\circ}$.

3.2. Heat transfer analysis

3.2.1 Overall heat transfer curves

From the time series, characteristic heat transfer curves are generated for the entire duration of the experiment for each inclination. Figure 4 shows the variations in heat flux q as a function of wall superheat $\Delta T = T_w - T_{sat}$ over the entire duration of the experiment for inclination of $\theta = 179^\circ$. This shows the cyclic behavior of heat transfer at the wall. Heat transfers differ according to each fluid regime. In the regime where the nucleation site is active (BER), the heat flux is maximal, $q = 960 \pm 40 \ W/m^2$, and the wall superheat is minimal, $\Delta T = 3.2 \pm 0.2^\circ C$. In the natural convection regime (LNC), the heat transfer is weaker, $q = 520 \ W/m^2$, and superheating is stronger, $\Delta T = 3.8^\circ C$.

The other points in the cycle correspond to transitions between the BER and LNC regimes. An entanglement between the different cycles is observed, revealing the existence of fluctuating behaviors at the boundary layer by the complex nature of the mechanisms involved. In the BER regime, bubbles nucleate, bubble volume increases and then it gets detached from the wall. This detachment generates high-amplitude fluid flow in the boundary layer. Once nucleation is deactivated, natural convection takes over (LNC). In these regimes, fluid motion at the wall takes place at different length scales. During the transition between these two regimes, there is coupling between these scales, giving rise to states that may differ from one cycle to the next.

Figure 4 (b) and (c) shows the characteristic heat transfer curves over several cycles for wall inclinations of 90° and 0°. As with the 179° inclination, we can see evidence of cyclic behavior. This is clearly identified for the 90° angle as well. Heat flux and superheat temperature at the wall are respectively $q = 940 \pm 10 \ W/m^2$, $\Delta T = 3.62 \pm 0.4$ °C for the BER regime. For the LNC regime, they are $q = 856 \pm 10 \ W/m^2$, $\Delta T = 3.94 \pm 0.04$ °C.

At an inclination of 0°, the two regimes are clearly distinguished by two distinct point clusters corresponding to the BER and LNC regimes. At this inclination, for the regime where the site is active, heat flux and superheat are respectively $q = 970 \pm 20 \, W/m^2$, $\Delta T = 3.65 \pm 0.1^{\circ}C$. When the site is inactive, heat flux and superheat are respectively $q = 960 \pm 20 \, W/m^2$, $\Delta T = 3.88 \pm 0.06^{\circ}C$. It should be noted that for this orientation, the temporal temperature signals show different patterns due to the sensors used. The temperature signal given by the thermocouple shows temperature variations of very low amplitudes (<0.05°C) and sudden temperature variations of higher amplitudes (0.15 to 0.3°C). The former is similar to noise, induced by the plumes in the LNC regime and by the bubble emissions in the BER regime, while those with higher amplitudes are the signature of the transition between the BER and LNC regimes. It should be noted that these transitions take place over short times (<0.4 s) with an unstable behavior. In addition, the duration of each phase is variable.

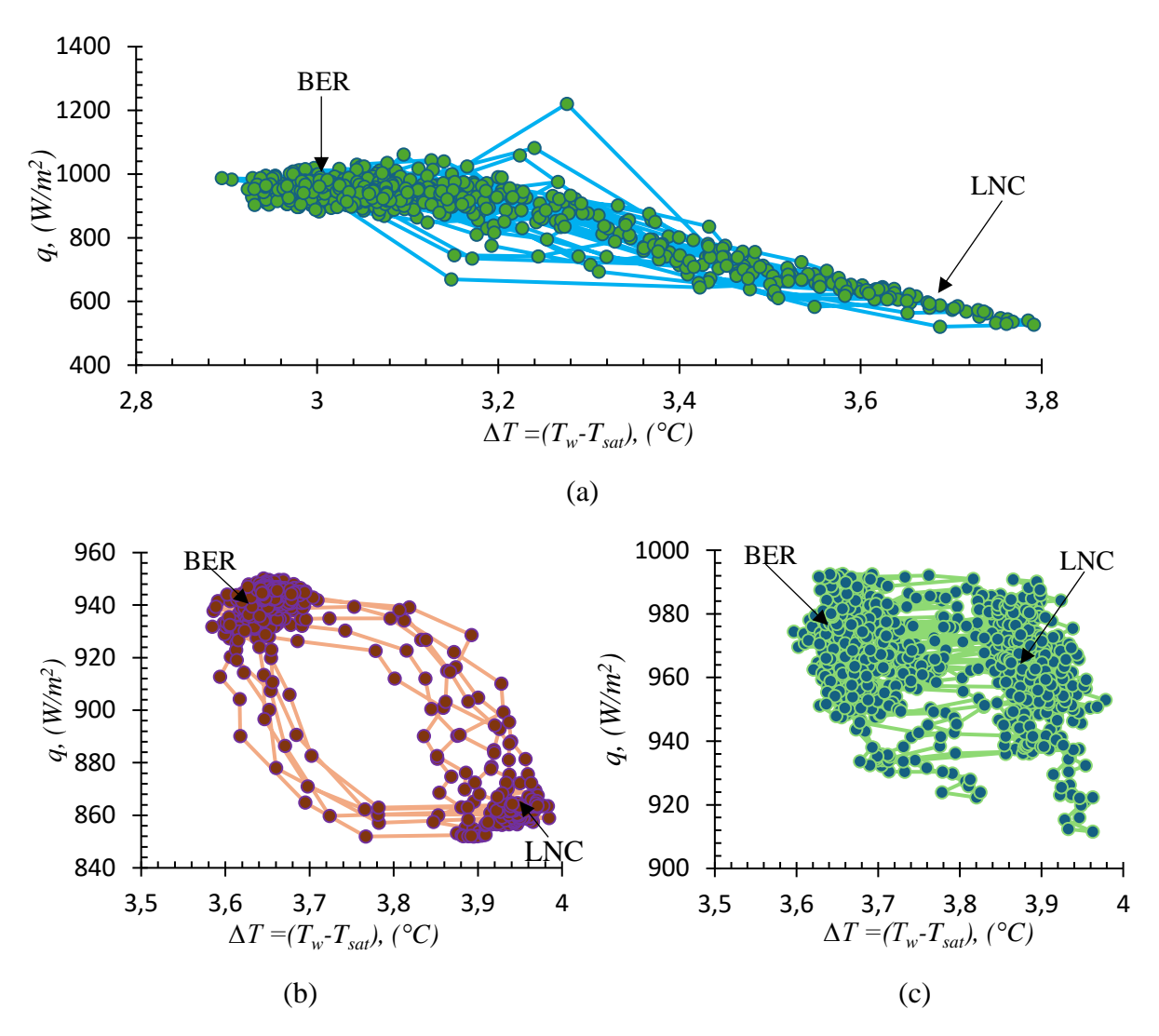


Figure 4 Heat transfer curves showing heat flux q with respect to temperature difference between wall temperature and liquid temperature $\Delta T = T_w - T_{sat}$ for a surface inclination (a) $\theta = 179^{\circ}$, (b) $\theta = 90^{\circ}$, (c) $\theta = 0^{\circ}$

3.2.2 Single heat transfer cycle

To better understand the transition between BER and LNC regimes, a single cycle for each orientation is investigated. Figure 5 (a) shows a single cycle for a wall inclination of 179°. The sequence relative to this cycle is that indicated between the points mentioned on the time series in Figure 3. The red point indicates the beginning of BER, while the black point marks the end of LNC. The direction of rotation of this cycle is clockwise. The cycle has an elongated shape, with large amplitudes of heat flux and temperature. The point density is characteristic of the relative duration of each regime. In this case, the BER regime is more persistent than the LNC regime. Similarly, the transition time from BER to LNC is longer ($\tau_{trBER-LNC} = 2.5s$) than the transition from LNC to BER ($\tau_{trLNC-BER} = 0.5s$).

Figure 5 (b) and (c) show the single cycles obtained for the 90° and 0° orientations. As for the 179° orientation, the direction of rotation of the cycle is clockwise. As before, the point density is characteristic of the duration of each regime. It should be noted that these transition times are governed by the behavior of the thermal boundary layer, and the boiling meter inertia.

These coupled phenomena therefore need to be taken into account when studying the heat transfer cycle.

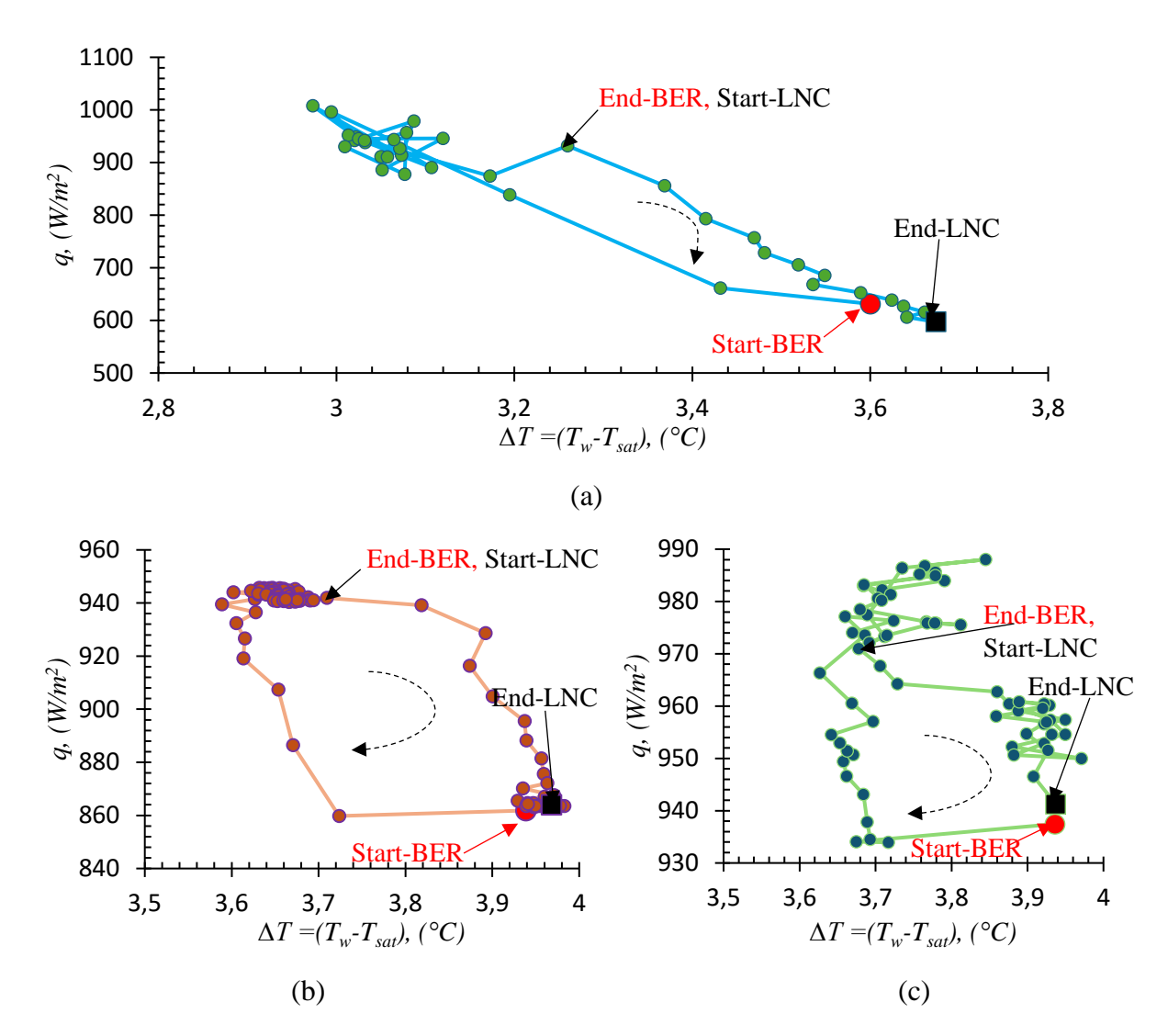


Figure 5 Heat transfer curves depicting heat flux q versus temperature difference between surface temperature and liquid temperature $\Delta T = T_w - T_{sat}$, showing one complete cycle from the initiation of bubble emission regime (BER) to the end of natural convection regime (LNC) for (a) $\theta = 179^\circ$, (b) $\theta = 90^\circ$, (c) $\theta = 0^\circ$. The dashed line with its arrow highlights the direction of the cycle.

To interpret the observed cyclic behavior, a simplified model based on an energy balance on a system composed by the boiling meter has been developed. This model is presented in Appendix 2. Three temperatures are introduced: \tilde{T} the average temperature of the boiling meter, T_{sup} is the temperature at the center of the active face of the boiling meter, and T_i is the average temperature at the rear face (the face opposite to the face with the nucleation site) of the boiling meter. We also introduce the three temperature differences: $\Delta T = T_{sup} - T_{sat}$; $\Delta T_i = T_i - T_{sat}$; $\Delta \tilde{T} = \tilde{T} - T_{sat}$.

The sign of the area S_c of the cycle $q_{sup} = f(\Delta T)$ is examined in the Appendix 2. q_{sup} is the average heat flux at the top face of the boiling meter, with the convention that it is positive when the heat is leaving the boiling meter. S_c is defined as:

$$S_c = \oint q_{sup} d \left(\Delta T \right) \tag{1}$$

The sign of S_c depends on the direction of rotation of the cycle. If this direction is clockwise then S_c is positive. To simplify the model, a linear relationship between the temperature differences $\Delta \widetilde{T}$, ΔT , and ΔT_i is assumed:

$$\Delta \tilde{T} = \alpha \Delta T \; ; \; \Delta T_i = \beta \Delta T \tag{2}$$

All these temperature differences refer to the difference of temperature with the temperature of the liquid T_{sat} far from the boiling meter. If the temperature differences inside the boiling meter are small compared to the temperature differences between its walls and the liquid, one can expect α and β to be positive and close to 1. The analysis in the Appendix 2 shows that for S_c to be positive, α must be negative. All experiments reported in the previous section (see Figure 7) exhibit a positive S_c , implying that α is negative. This suggest that ΔT and $\Delta \tilde{T}$ vary in opposite directions: when ΔT increases, $\Delta \tilde{T}$ decreases, and vice versa. This is counterintuitive, as one might expect a positive α , indicating that \tilde{T} and T_{sup} vary similarly. Consequently, α cannot be considered constant over the whole time of a cycle. Equation (A.9) - given in Appendix 2- shows that if α and β remain positive and vary with time, S_c can still be positive. While a detailed analysis of heat transfer inside the boiling meter is beyond the scope of this paper, we note that T_{sup} , \tilde{T} and T_i must exhibit distinct temporal behaviors during a cycle.

The behavior of a cycle can be explained by the following steps, starting from the beginning of the LNC regime:

- The liquid in the region of the active face of the boiling meter is heated and its temperature increases until it reaches the nucleation temperature. It is worth noting that for the 3 orientations (0°, 90° and 179°), the end of the LNC regime occurs at a similar value of ΔT in the order of 3.9 °C. This means that the departure from the LNC regime is mainly governed by the nucleation temperature at the nucleation site.
- The end of the LNC regime and the beginning of the BER regime correspond to the instant when the nucleation of a bubble starts. Then a transient phase begins for commuting from the LNC to the BER regime. During this transient phase, due to the emission of bubbles and to the resulting enforcement of the liquid motion, the wall temperature T_{sup} decreases and the heat flux q_{sup} increases. As q_{sup} increases, the average temperature \tilde{T} decreases. Thus, when the BER regime is reached at the end of this transient phase, the value of \tilde{T} is lower than during the LNC regime.
- During the BER regime, q_{sup} is stable in average, but due to its higher value than during the LNC regime, \tilde{T} continues to decrease. One can consider that q_{sup} is proportional to the temperature difference $\tilde{T}-T_{sup}$, It results from this decrease of \tilde{T} (as T_{sup} does not vary), that q_{sup} will start to decrease until the value of the heat flux at the wall becomes too low to maintain the emission of bubbles. At that time the BER period is finished.

Then a transition phase from the BER to the LNC starts during which both T_{sup} and \tilde{T} increase.

This analysis highlights two key criteria for cycle progression: - the wall temperature threshold for bubble nucleation; - the heat flux threshold needed to sustain bubble emission. It is thus understandable why the BER regime remains stable for the 180° orientation: the heat flux during this phase does not fall below the threshold required for continued bubble generation.

3.3. Heat transfer coefficient

To quantify heat transfer close to the wall, we need to determine the heat transfer coefficient. This value can be obtained by measuring heat flux and temperatures at the wall, and in the fluid. In the present study, the boiling meter is instrumented with a heat flux sensor located 200 μm below the wall and a temperature sensor located 100 μm below the wall. As mentioned in section 2, the wall temperature corresponds to a local measurement whereas the heat flux sensor measures the heat flux across the entire surface of the boiling meter in contact with the wall. The heat transfer coefficient is defined as:

$$h = \frac{q}{T_W(r=0) - T_{sat}} \tag{4}$$

where r=0 corresponds to the center of the boiling surface. The purpose of evaluating this parameter is not to propose a correlation, but rather to compare heat transfer in the presence and absence of an active nucleation site, and for different wall orientations. However, for information purposes, the data obtained can be compared with literature data when available. This is the case for the natural convection regime. On the contrary, for the single-site boiling regime, these data are original and therefore cannot be compared with literature data.

Figure 6 shows, for a wall inclination of 179° , the variations of the heat transfer coefficient for a time interval ranging from 10 to 70s. During this interval, the BER and LNC regimes follows one another. For the BER regime, the heat transfer coefficient is close to $h_{BER}(179^{\circ}) = 320 \pm 20 \, W/m^{2 \circ} C$. In the LNC regime, steady state is not reached. In some cases, it just started, while in others, the regime is well underway but never reached. In the case where it is well underway, the heat transfer coefficient is close to $h_{LNC}(179^{\circ}) = 175 \pm 10 \, W/m^{2 \circ} C$; and if it's just primed, it can reach $h_{LNC}(179^{\circ}) = 260 \pm 10 \, W/m^{2 \circ} C$. For another series of experiments, where both regimes are reached, the exchange coefficients are $h_{BER}(179^{\circ}) = 275 \pm 20 \, W/m^{2 \circ} C$ and $h_{LNC}(179^{\circ}) = 130 \pm 10 \, W/m^{2 \circ} C$ (Figure 6 (b)).

Similar behaviors are observed for inclinations of 90° and 0° . Figure 7 (a) and (b) show the heat transfer coefficient variations as a function of time. For each inclination, the heat transfer coefficients differ according to the regime. Time intervals during which both regimes are present are shown for wall inclinations of 90° and 0° . As in the previous case, the heat transfer coefficients differ according to the regime.

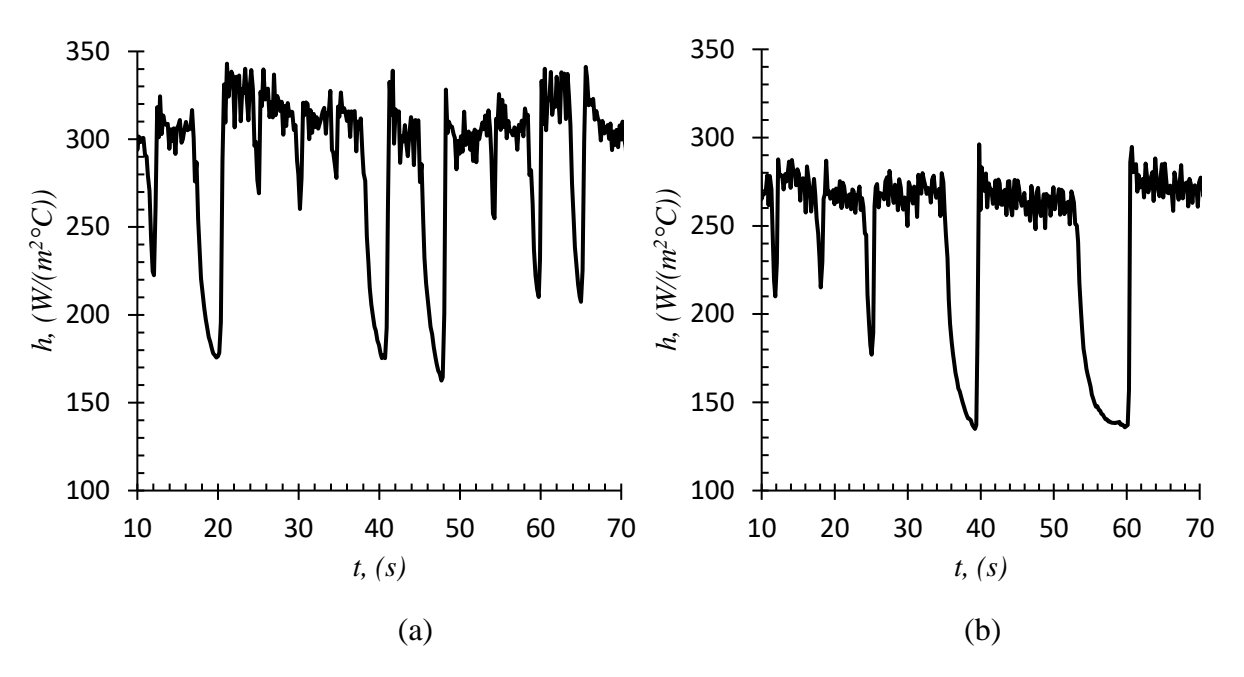


Figure 6 Heat transfer coefficient as a function of time for the 179° wall inclination. The first (a) corresponds to the situation where the 179° tilt is obtained just after initiating nucleation activation at 180° . The second (b) corresponds to the case where this inclination is obtained after going back and forth 180° - 0° - 180° .

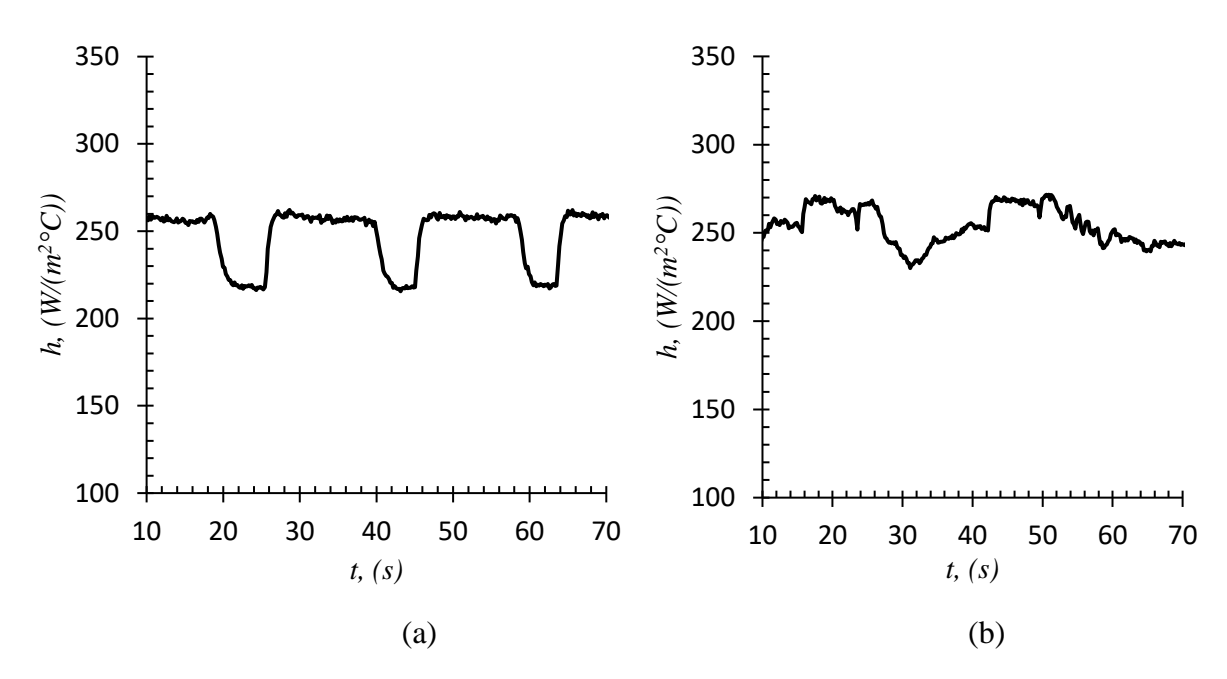


Figure 7 Heat transfer coefficient h as a function of time t for (a) 90° and (b) 0° orientation

Average heat transfer coefficient (h) as a function of the inclination (θ) is presented in the Figure 8. The figure displays three h values for each inclination: the average h in BER, the average h in LNC, and the h in natural convection regime at different inclinations, from Tadrist et al. [34]. For BER, h ranges from $300-340~W/m^2°C$ at 179°, $254-260~W/m^2°C$ at 90°, and $253-273~W/m^2°C$ at 90°. In LNC, h varies between $137-270~W/m^2°C$ at 179°, $216-222~W/m^2°C$ at 90°, and $230-250~W/m^2°C$ at 90°. In BER, h increases with θ , whereas in LNC,

the opposite trend is observed. The standard deviation values indicate lower variations in h at 0° (9%) and 90° (17%), while at 179° , the difference between BER and LNC is significantly higher (90%).

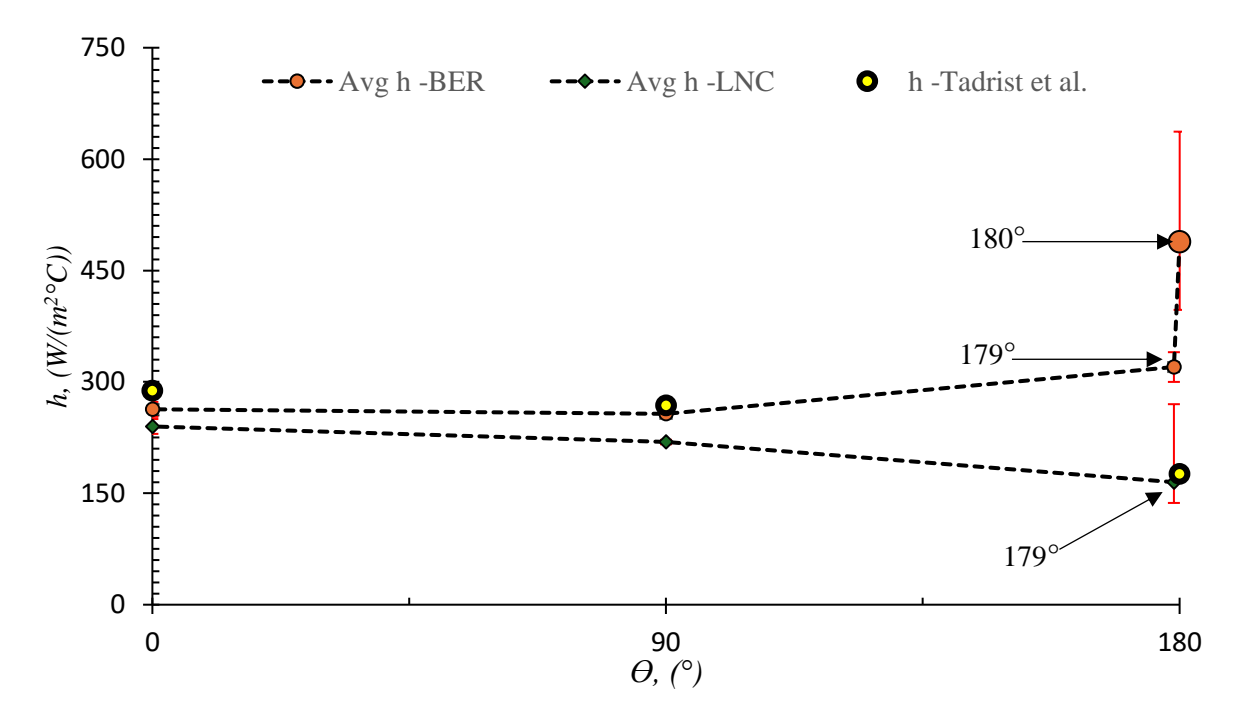


Figure 8 Average heat transfer coefficient for BER, LNC and for different surface inclination θ , and comparison of LNC (present work) with natural convection values from Tadrist et al. [34] at different inclinations

To interpret the heat transfer results obtained, we have combined observations with thermal measurements. In the LNC regime, the fluid remains in the liquid state, and shadowgraphy method (conducted by illuminating the cell from the back and observing from the front) reveals natural convection movements in the form of a plume when the wall orientation is 0° [33]. Similar movements are also observed at 90° and 179° [39,40]. Their demonstration is more difficult to achieve, given the low liquid speed involved in the experiments.

It is also necessary to consider the different characteristic times of the bubble emission time τ_b , the bubble emission regime τ_{BER} and the natural convection regime τ_{LNC} . Table 1 gives an estimate of these times. Note that these times corresponding to each regime (τ_{BER} , τ_{LNC}) decrease as the angle increases. The opposite behavior is observed for the bubble emission time. It always remains well below the times relative to each of the regimes.

From these data, it is possible to qualitatively interpret the mechanisms governing the heat transfer at the wall. Under natural convection, the thermal boundary layer depends on the Rayleigh number [41]. Comparison with literature correlations gives similar trends, albeit with significant discrepancies. Comparison with data from the same experiment [34] gives close values. As soon as bubble nucleation takes place, the thermal boundary layer is modified. The transition times between the LNC and BER regimes are shown in Table 1. They differ according to the wall inclination. They are correlated with the coupled heat transfer phenomena between the fluid and the boiling meter.

4. Conclusion

The experimental set up using a boiling meter is able to measure the temperature and heat flux evolutions at the wall. The degree of sensitivity of the temperature and heat flux sensors allows the heat transfer analysis at the transition between the natural convection and nucleate boiling regime. An intermittent behavior has been observed across various wall inclination angles, characterized by alternating phases of natural convection and bubble emission. This phenomenon persists whatever is the wall orientation in the range 0° -179°. To our knowledge, this phenomenon has never been reported in the literature. This intermittency is highlighted with a limit cycle in the frame of heat flux versus temperature difference between wall and saturated liquid temperature. Two criteria are found to control this intermittency: the wall temperature threshold for bubble nucleation and the heat flux threshold needed to sustain bubble emission.

The impact of this intermittence on heat flux and wall temperature is emphasized. It is observed that the difference in heat flux between the two regimes at a 179° inclination is approximately 41%. This disparity decreases with lower inclination angles; at 90°, the difference drops to 7%, and at 0°, the variation in heat flux becomes negligible due to the minimal contribution of individual bubbles to the overall heat flux.

This approach has enabled us to evaluate the heat transfer coefficient h for different wall inclinations. We have shown that the intensity of heat transfer, through the heat transfer coefficient, depends on the wall orientation for both the natural convection regime - LNC - and the bubble emission regime -BER. In BER, the heat transfer coefficient h increases with inclination angle, whereas in LNC, the opposite trend is observed. For BER, the average h is $263 \ W/m^2 \,^{\circ}C$ at 0° , $257 \ W/m^2 \,^{\circ}C$ at 90° , and rises to $320 \ W/m^2 \,^{\circ}C$ at 179° ; in contrast, for LNC, h decreases from $240 \ W/m^2 \,^{\circ}C$ at 0° to $219 \ W/m^2 \,^{\circ}C$ at 90° , and further to $203 \ W/m^2 \,^{\circ}C$ at 179° . The largest difference between the two regimes occurs at 179° , reaching $\sim 57\%$, while even at 0° , a notable $\sim 10\%$ difference is observed despite the small size of vapor bubbles relative to the wall.

In order to account for the behavior of the heat transfer cycle, more detailed modelling of conjugated heat transfers in the fluid and the boiling meter will be developed, and constitutes one of the perspectives of this work. The second perspective concerns the study of bubble activation and extinction mechanisms. This last perspective opens a new area. The latter perspective would provide a better understanding of the mechanisms involved in triggering boiling at an isolated site.

Acknowledgement

The authors acknowledge the ANR – FRANCE (French National Research Agency) for its financial support of the TraThI project ANR-21-CE50-0009-01. LT acknowledges the CNES (National Centre for Space Studies) for its financial support of the project ERAMEN. This work has been achieved in the frame of the EIPHI Graduate school (contract "ANR-17-EURE-0002").

References

- [1] Long J, Liu Z, Cao Z, Wu J, Xie X. Highly efficient pool boiling heat transfer on surfaces with zoned rose-petal-inspired hierarchical structures. Appl Therm Eng 2024;241:122330. https://doi.org/10.1016/J.APPLTHERMALENG.2023.122330.
- [2] Zhu C, Zhang L, Zhang D, Wang Z, Qian L, Jiang Z. Effect of micro-cavities structured surfaces on bubble dynamics and pool boiling heat transfer enhancement. Appl Therm Eng 2025;270:126220. https://doi.org/10.1016/J.APPLTHERMALENG.2025.126220.
- [3] Sun X, Li Q, Liu B, Chang H. Composite microstructured surface with micro-cavities and micro-ditches on micro-pin-fins for enhancing pool boiling heat transfer. Appl Therm Eng 2024;252:123713. https://doi.org/10.1016/J.APPLTHERMALENG.2024.123713.
- [4] Sun Y, Li H, Chen J, Wu C, Tang H, Zhang S, et al. Hierarchical sintered porous surfaces with enhanced pool boiling heat transfer performance for high-power cooling applications. Appl Therm Eng 2024;249:123368. https://doi.org/10.1016/J.APPLTHERMALENG.2024.123368.
- [5] Dadjoo M, Etesami N, Esfahany MN. Influence of orientation and roughness of heater surface on critical heat flux and pool boiling heat transfer coefficient of nanofluid. Appl Therm Eng 2017;124:353–61. https://doi.org/10.1016/j.applthermaleng.2017.06.025.
- [6] Li Q, Zhao J, Sun X, Liu B. Experimental investigation of pool boiling heat transfer on pillar-structured surfaces with different wettability patterns. Appl Therm Eng 2022;215:118924. https://doi.org/10.1016/J.APPLTHERMALENG.2022.118924.
- [7] Zupančič M, Steinbücher M, Gregorčič P, Golobič I. Enhanced pool-boiling heat transfer on laser-made hydrophobic/superhydrophilic polydimethylsiloxane-silica patterned surfaces. Appl Therm Eng 2015;91:288–97. https://doi.org/10.1016/J.APPLTHERMALENG.2015.08.026.
- [8] Wang X, Xu J, Jiang H, Liu Y, Li X, Shan D, et al. Achieving robust and enhanced pool boiling heat transfer using micro–nano multiscale structures. Appl Therm Eng 2023;227:120441. https://doi.org/10.1016/J.APPLTHERMALENG.2023.120441.
- [9] Liang G, Mudawar I. Review of pool boiling enhancement with additives and nanofluids. Int J Heat Mass Transf 2018;124:423–53. https://doi.org/10.1016/J.IJHEATMASSTRANSFER.2018.03.046.
- [10] Ali HM, Generous MM, Ahmad F, Irfan M. Experimental investigation of nucleate pool boiling heat transfer enhancement of TiO2-water based nanofluids. Appl Therm Eng 2017;113:1146–51. https://doi.org/10.1016/J.APPLTHERMALENG.2016.11.127.
- [11] Deng D, Wan W, Feng J, Huang Q, Qin Y, Xie Y. Comparative experimental study on pool boiling performance of porous coating and solid structures with reentrant channels. Appl Therm Eng 2016;107:420–30. https://doi.org/10.1016/J.APPLTHERMALENG.2016.06.172.
- [12] Zhong D, Lian X, Shi H, Zhang J, Meng J, Zhang J. Enhancement of the critical heat flux for downward-facing saturated pool boiling on the reticular hollow shell structure

- surfaces. Appl Therm Eng 2024;236:121635. https://doi.org/10.1016/j.applthermaleng.2023.121635.
- [13] Petrovic MM, Stevanovic VD. Pool boiling simulation with two-fluid and grid resolved wall boiling model. International Journal of Multiphase Flow 2021;144:103806. https://doi.org/10.1016/J.IJMULTIPHASEFLOW.2021.103806.
- [14] Di Marco P, Grassi W, Memoli G. Experimental study on rising velocity of nitrogen bubbles in FC-72. International Journal of Thermal Sciences 2003;42:435–46. https://doi.org/10.1016/S1290-0729(02)00044-3.
- [15] Vazquez A, Sanchez RM, Salinas-Rodríguez E, Soria A, Manasseh R. A look at three measurement techniques for bubble size determination. Exp Therm Fluid Sci 2005;30:49–57. https://doi.org/10.1016/J.EXPTHERMFLUSCI.2005.03.018.
- [16] Moghaddam S, Kiger K. Physical mechanisms of heat transfer during single bubble nucleate boiling of FC-72 under saturation conditions-I. Experimental investigation. Int J Heat Mass Transf 2009;52:1284–94. https://doi.org/10.1016/j.ijheatmasstransfer.2008.08.018.
- [17] Li J, Yang Z, Duan Y. Experimental study on single bubble growth of R32 + R1234yf binary mixtures during saturated pool boiling. Appl Therm Eng 2023;219:119535. https://doi.org/10.1016/J.APPLTHERMALENG.2022.119535.
- [18] Kumar A, Abubakr B, Srivastava A. Non-intrusive experiments on coupled bubble dynamics and heat transfer during nucleate boiling under varying pressure conditions. Appl Therm Eng 2025;261:125102. https://doi.org/10.1016/J.APPLTHERMALENG.2024.125102.
- [19] van Stralen SJD, Cole R, Sluyter WM, Sohal MS. Bubble growth rates in nucleate boiling of water at subatmospheric pressures. Int J Heat Mass Transf 1975;18:655–69. https://doi.org/10.1016/0017-9310(75)90277-X.
- [20] Kim J, Huh C, Kim MH. On the growth behavior of bubbles during saturated nucleate pool boiling at sub-atmospheric pressure. Int J Heat Mass Transf 2007;50:3695–9. https://doi.org/10.1016/j.ijheatmasstransfer.2006.11.049.
- [21] Rogers TF, Mesler RB. An experimental study of surface cooling by bubbles during nucleate boiling of water. AIChE Journal 1964;10:656–60. https://doi.org/10.1002/aic.690100516.
- [22] Hendricks RC, Sharp RR. Initiation of cooling due to bubble growth on a heating surface. National Aeronautics and Space Administration; 1964.
- [23] Tsai J-H, Lin L. Transient Thermal Bubble Formation on Polysilicon Micro-Resisters. J Heat Transfer 2002;124:375–82. https://doi.org/10.1115/1.1445136.
- [24] Demiray F, Kim J. Microscale heat transfer measurements during pool boiling of FC-72: effect of subcooling. Int J Heat Mass Transf 2004;47:3257–68. https://doi.org/10.1016/j.ijheatmasstransfer.2004.02.008.
- [25] Myers JG, Yerramilli VK, Hussey SW, Yee GF, Kim J. Time and space resolved wall temperature and heat flux measurements during nucleate boiling with constant heat flux

- boundary conditions. Int J Heat Mass Transf 2005;48:2429–42. https://doi.org/10.1016/j.ijheatmasstransfer.2004.12.050.
- [26] Golobic I, Petkovsek J, Baselj M, Papez A, Kenning DBR. Experimental determination of transient wall temperature distributions close to growing vapor bubbles. Heat and Mass Transfer 2009;45:857–66. https://doi.org/10.1007/s00231-007-0295-y.
- [27] Yabuki T, Nakabeppu O. Heat transfer mechanisms in isolated bubble boiling of water observed with MEMS sensor. Int J Heat Mass Transf 2014;76:286–97. https://doi.org/10.1016/j.ijheatmasstransfer.2014.04.012.
- [28] Jung S, Kim H. An experimental method to simultaneously measure the dynamics and heat transfer associated with a single bubble during nucleate boiling on a horizontal surface. Int J Heat Mass Transf 2014;73:365–75. https://doi.org/10.1016/j.ijheatmasstransfer.2014.02.014.
- [29] Li Z-D, Zhang L, Zhao J-F, Li H-X, Li K, Wu K. Numerical simulation of bubble dynamics and heat transfer with transient thermal response of solid wall during pool boiling of FC-72. Int J Heat Mass Transf 2015;84:409–18. https://doi.org/10.1016/j.ijheatmasstransfer.2014.12.061.
- [30] Li J, Yang Z, Duan Y. Numerical simulation of single bubble growth and heat transfer considering multi-parameter influence during nucleate pool boiling of water. AIP Adv 2021;11. https://doi.org/10.1063/5.0065877.
- [31] Cao Z, Zhou J, Wei J, Sun D, Yu B. Experimental and numerical study on bubble dynamics and heat transfer during nucleate boiling of FC-72. Int J Heat Mass Transf 2019;139:822–31. https://doi.org/10.1016/j.ijheatmasstransfer.2019.05.061.
- [32] Kunkelmann C, Ibrahem K, Schweizer N, Herbert S, Stephan P, Gambaryan-Roisman T. The effect of three-phase contact line speed on local evaporative heat transfer: Experimental and numerical investigations. Int J Heat Mass Transf 2012;55:1896–904. https://doi.org/10.1016/j.ijheatmasstransfer.2011.11.044.
- [33] Zamoum M, Tadrist L, Combeau H, Kessal M. Experimental Study of Boiling Heat Transfer on Multiple and Single Nucleation Sites Using a Boiling-Meter. Heat Transfer Engineering 2014;35:508–16. https://doi.org/10.1080/01457632.2013.833052.
- [34] Tadrist L, Combeau H, Zamoum M, Kessal M. Experimental study of heat transfer at the transition regime between the natural convection and nucleate boiling: Influence of the heated wall tilt angle on the onset of nucleate boiling (ONB) and natural convection (ONC). Int J Heat Mass Transf 2020;151:119388. https://doi.org/10.1016/J.IJHEATMASSTRANSFER.2020.119388.
- [35] Kharkwal H, Zamoum M, Barthés M, Lanzetta F, Combeau H, Tadrist L. Vapor bubble on a single nucleation site: Temperature and heat flux measurements. J Phys Conf Ser 2024;2766:012148. https://doi.org/10.1088/1742-6596/2766/1/012148.
- [36] Captec n.d. https://www.captec.fr/copie-de-fluxmetre-thermique (accessed March 9, 2025).

- [37] Thery P, Leclercq D, Herin P. Device for measuring the intensity of a radiative flux and optionally also measuring the intensity of a convective flux 1989.
- [38] 3M TM. https://multimedia.3m.com/mws/media/64892O/3m-fluorinert-electronic-liquid-fc72-en.pdf n.d.
- [39] Incropera FP, DeWitt DP, Bergman TL, Lavine AS. Fundamentals of heat and mass transfer. vol. 6. Wiley New York; 1996.
- [40] Zaite A, Kharkwal H, Barthés M, Lanzetta F, Combeau H, Tadrist L. Thermal characterisation of a boiling meter using experiment and numerical simulation in a boiling cell. International Days on Thermal Science and Energy, Paris: 2024, p. 29–31.
- [41] Kim N, Schindler F, Vogt T, Eckert S. Thermal boundary layer dynamics in low-Prandtl-number Rayleigh–Bénard convection. J Fluid Mech 2024;994:A4. https://doi.org/10.1017/jfm.2024.629.

Appendix 1: Uncertainty quantification

The type A uncertainty derived from only 3 measurements per temperature point exhibits relatively high values as statistical uncertainty decreases proportionally to $1/\sqrt{n}$ (reflecting the limited degrees of freedom n-1 = 2): the Student's k-coefficient $k_{0.05,2} = 4.30$ for a 95% confidence level. We should have taken at least 10 measurements per temperature point, but this was not possible in our experiments. In such a case, for 10 measurements, the Student's k-coefficient, for a 95% confidence level, would have been lower ($k_{0.05,9} = 2.262$) and the uncertainty calculation would have been much more relevant and consistent from a statistical point of view.

Type B uncertainty is employed when repeated measurements are not available to statistically assess dispersion. It is evaluated using information derived from sources (other than statistical analysis of observational data series. For this reason, we decided to calculate the type B uncertainty as follow:

In our experiments, the temperatures are measured with a type-T thermocouple connected to a Data Acquisition system (DAQ) and compared with those measured by the Pt100 sensor for the calibration.

1) High precision type-T thermocouple:

Precision =
$$\pm 0.20$$
°C

Uncertainty:
$$u_T = \frac{Precision}{\sqrt{3}} = \frac{0.20}{\sqrt{3}} = 0.115$$
°C

2) Pt100, class AA (IEC-60751):

tolerance =
$$\pm 0.10 + 0.0017 \times T$$

If we assume that the maximum temperature is 60° C in our experiments, the corresponding tolerance is equal to $\pm 0.10 + 0.0017 \times 60 = 0.202^{\circ}$ C

Uncertainty:
$$u_{Pt100} = \frac{Tolerance\ at\ 60^{\circ}C}{\sqrt{3}} = \frac{0.202}{\sqrt{3}} = 0.1166^{\circ}C$$

The resolution of the Pt100 electronic material is given: $resolution_{matPt100} = 0.001^{\circ}C$

Uncertainty:
$$u_{matPt100} = \frac{\text{resolutionmatPt100}}{\sqrt{3}} = \frac{0.001}{\sqrt{3}} = 0.00058^{\circ}C$$

The self-heating of the Pt100 is negligible and $u_{selfPt100} \approx 0^{\circ}C$

3) DAQ system (Agilent Benchlink acquisition software)

Resolution = 0.06°C

Uncertainty:
$$u_{DAQ} = \frac{Resolution}{2\sqrt{3}} = \frac{0.06}{2\sqrt{3}} = 0.01732$$
°C

4) The experiments were conducted during 2 months and the temporal drift need to be considered.

The annual drift is given as a mean value ± 0.005 °C/year.

Uncertainty:
$$u_{drift} = \frac{Annual\ drift \times \frac{number\ of\ months}{12\ months/year}}{\sqrt{3}} = \frac{0.005 \times \frac{2}{12}}{\sqrt{3}} = 0.000481^{\circ}C$$

5) The two temperature sensors (the Pt100 sensor and the type-T thermocouple) are close together, but we could consider a temperature gradient ΔT between them: $\Delta T = 0.1^{\circ}C$ (it is difficult to estimate it).

Uncertainty:
$$u_{\Delta T} = \frac{\Delta T}{\sqrt{3}} = \frac{0.1}{\sqrt{3}} = 0.0577^{\circ}C$$

6) The combined uncertainty of the type-T thermocouple is

$$u_{\text{comb-Type-T}} = \sqrt{u_T^2 + u_{DAQ}^2 + u_{drift}^2} = \sqrt{0.115^2 + 0.01732^2 + 0.000481^2} = 0.1162^{\circ}C$$

7) The combined uncertainty of the Pt100 sensor is

$$u_{\text{comb-Pt100}} = \sqrt{u_{Pt100}^2 + u_{matPt100}^2 + u_{drift}^2 + u_{selfPt100}^2}$$
$$= \sqrt{0.1166^2 + 0.00058^2 + 0.000481^2 + 0} = 0.1166^{\circ}C$$

8) Finally, the total type-B uncertainty of the temperature measurement system compares the two sensors and:

$$u_{\rm B} = \sqrt{u_{\rm comb-Type-T}^2 + u_{\rm comb-Pt100}^2 + u_{\Delta T}^2} = \sqrt{0.1162^2 + 0.1166^2 + 0.0577^2}$$

= 0.17°C \approx 0.2°C

The total type-B uncertainty in temperature measurement is 0.2 °C

Appendix 2: Heat transfer model for the boiling meter

In order to analyze a cycle, a model describing the heat transfer in the boiling meter has been derived. This model is described in this appendix. The system that we consider for the energy balance is the whole boiling meter. Conduction is the only mode of heat transfer inside the

boiling meter. Moreover, we assume that there is no heat loss from the lateral side of the boiling meter and that the heat flux at its rear face (the opposite face to the face with the nucleation site) can be described by a heat transfer coefficient, as there is only natural convection active at this face. By integrating the heat transfer equation on the volume of the boiling meter, the energy balance can be written as follows:

$$mC_p \frac{d\tilde{r}}{dt} = -q_{sup}S - h_i S(T_i - T_{sat}) + \varphi_e S$$
 (A.1)

where:

 \tilde{T} is the average temperature of the boiling meter;

m, C_p are the mass and average heat capacity, respectively, of the boiling meter;

 q_{sup} is the average heat flux at the top face of the boiling meter, with the convention that it is positive when the heat is leaving the boiling meter;

 h_i is the transfer coefficient on the rear face of the boiling meter;

S is the area of the top or bottom faces of the boiling meter;

 φ_e is the heat flux generated by joule effect in the boiling meter, φ_e S is equal to the electric heat power imposed to the heater;

 T_i is the temperature of the wall at rear face of the boiling meter and T_{sat} the saturation temperature of the fluid

The area of the cycle $q_{sup} = f(\Delta T)$ as presented in section 3.2.2 has the following expression:

$$S_c = \oint q_{sup} d(\Delta T) \tag{A.2}$$

Introducing the time t, the area of the cycle can be expressed thanks to a change of variable as:

$$S_c = \int_0^{t_c} q_{sup} \frac{d(\Delta T)}{dt} dt$$
 (A.3)

where t_c is the time duration of the cycle. We can define the following temperature differences:

$$\Delta T = T_{sup} - T_{sat}; \ \Delta T_i = T_i - T_{sat}; \ \Delta \widetilde{T} = \widetilde{T} - T_{sat} \ (A.4)$$

where T_{sup} is the average temperature of the wall at the top face of the boiling meter

Using these new variable, Equation (A.1) becomes:

$$\frac{mc_p}{S}\frac{d(\Delta \tilde{T})}{dt} = -q_{sup} - h_i \Delta T_i + \varphi_e \tag{A.5}$$

By replacing q_{sup} by its expression in equation (A.5), equation (A.3) becomes:

$$S_c = \int_0^{t_c} -\left[\frac{mc_p}{S}\frac{d(\Delta \tilde{T})}{dt} + h_i \Delta T_i\right] \frac{d(\Delta T)}{dt} dt + \int_0^{t_c} \varphi_e \frac{d(\Delta T)}{dt} dt$$
 (A.6)

As the value of ΔT is the same at the beginning and at the end of the cycle and φ_e is constant the last term on the right of equation (A.6) is equal to zero: $\int_0^{t_c} \varphi_e \frac{d(\Delta T)}{dt} dt = \varphi_e [\Delta T]_0^{t_c} = 0.$ Therefore, equation (A.6) simplifies as:

$$S_c = -\int_0^{t_c} \left[\frac{mc_p}{S} \frac{d(\Delta \tilde{T})}{dt} + h_i \Delta T_i \right] \frac{d(\Delta T)}{dt} dt$$
 (A.7)

To test the way the temperature in the boiling meter evolves during a cycle we assume a simple relation between the temperature differences which is to consider that a relation of proportionality exists between them:

$$\Delta \tilde{T} = \alpha \Delta T \; ; \; \Delta T_i = \beta \Delta T \tag{A.8}$$

One can consider that α and β reflect in average how $\Delta \tilde{T}$ and ΔT_i vary when ΔT varies. If α respectively β is positive, it means that in average during one cycle, $\Delta \tilde{T}$ respectively ΔT_i varies in the same way than ΔT . In other word it means that if ΔT increases then $\Delta \tilde{T}$ respectively ΔT_i increases also.

Thus, Equation (A.7) becomes:

$$S_c = -\int_0^{t_c} \frac{mc_p}{S} \alpha \left[\frac{d(\Delta T)}{dt} \right]^2 dt - \int_0^{t_c} h_i \beta \Delta T \frac{d(\Delta T)}{dt} dt$$
 (A.9)

The second term of the right side of this equation is equal to zero as:

$$\int_0^{t_c} h_i \beta \Delta T \frac{d(\Delta T)}{dt} dt = \frac{h_i \beta}{2} [\Delta T^2]_0^{t_c} = 0$$
 (A.10)

Therefore equation (9) becomes:

$$S_c = -\alpha \frac{mc_p}{S} \int_0^{t_c} \left[\frac{d(\Delta T)}{dt} \right]^2 dt$$
 (A.11)

As we can see, from equation (A.11), the area of the cycle can only be positive if:

$$\alpha \frac{mc_p}{s} \int_0^{t_c} \left[\frac{d(\Delta T)}{dt} \right]^2 dt < 0 \tag{A.12}$$

As the integral is positive, α needs to be negative. Which means that in this case ΔT and $\Delta \tilde{T}$ vary in an opposite way.